

PROBING THE HISTORY OF SOLAR SYSTEM THROUGH THE CRATERING RECORDS ON VESTA AND CERES

TURRINI D., MAGNI G., AND CORADINI A.

ABSTRACT. Dawn space mission will provide the first, detailed data of two of the major bodies in the Main Belt, Vesta and Ceres. In the framework of our studies on the origin of Solar System, we modelled the accretion of Jupiter and, through an N-Body code developed on purpose, we evaluated the flux of impactors on Vesta and Ceres keeping track of their formation zones. We also studied the effects of the possible inward migration of Jupiter on the rate and the characteristics of the impacts. We here describe the different scenarios and their implications for the evolution of Solar System.

1. INTRODUCTION

Dawn mission will provide detailed images of Vesta and Ceres surfaces and supply crucial information to constrain their mineralogical and elemental composition through VIR, its imaging spectrometer. Thanks to these data, we will be able to study in depth the crater record on the surface of both Vesta and Ceres. We discuss here our study of the cratering process of Vesta and Ceres at the time of Jupiter formation. In our model we consider Jupiter's gas accretion and displacement due to angular momentum exchange with the surrounding nebula. The gas accretion model used has been described in Coradini et al. (2004). Jupiter's migration has been included to estimate the effect of increasing displacements.

2. DYNAMICAL AND PHYSICAL MODEL

To explore the early collisional history of Vesta and Ceres we simulated the dynamical evolution of a section of the young Solar System at the time of Jupiter's core formation and the subsequent accretion of the gaseous envelope. Our template of the forming Solar System was composed of the Sun, the accreting Jupiter and a swarm of massless particles representing the planetesimals. The massless particles were initially distributed into a limited spatial region, which has been chosen to optimise the computational requirements after a set of numerical experiments aiming

Key words and phrases. Ceres, Vesta, Main Belt, Jupiter, Solar System formation, N-Body methods.

to determine the region of Solar System influenced by the forming Jupiter on the considered timespan. Being interested on the effects of Jupiter's mass increase on the dynamical stability and the evolution of the Solar System, we didn't model the giant planet formation process directly through hydrodynamical computations. In our simulations we reproduced the evolution of Jupiter through an analytical approach: the parameters on which the model was based, however, were derived from the results of hydrodynamical simulations performed with the code described in Coradini et al. (2004). During the dynamical evolution of our template of the Solar System we evaluated through a statistic approach the probability of planetesimals impacting against Vesta and Ceres. In the following subsections we will describe in detail the initial conditions and the physical parameters and constraints of the model.

2.1. Jupiter's formation and migration. In our analytical approach, we considered Jupiter's formation as composed by 3 different stages:

- a first core accretion phase;
- a second exponential gas accretion phase;
- a final phase of asymptotic gas accretion.

At the beginning of the simulations, Jupiter is an embryo with mass $M_0 = 0.1 M_{\oplus}$ growing on a time $\tau_c = 3 \times 10^5$ years to the critical mass $M_c = 15 M_{\oplus}$. The mass growth is governed by the equation

$$(1) \quad M_p = M_0 + \left(\frac{e}{e-1} \right) (M_c - M_0) \times \left(1 - e^{t/\tau_c} \right)$$

The timescale for core accretion, smaller than what the theoretical models for giant planet formation predict, has been chosen to limit the computational load of the simulations. During the first stage of accretion, Jupiter's core mass is negligible in terms of its perturbing effects on the planetesimals in the disk and the only planetesimals affected by Jupiter are those which undergo a close encounter with the forming planet. As a consequence, in this phase the number of impacts against the considered asteroids is governed by stochastic collisions and is a linear function of time: we can approximate the evolution on a longer timescale by extrapolating from our results.

After Jupiter's core reached the critical mass value of $15 M_{\oplus}$, the nebular gas surrounding it becomes gravitationally unstable and starts to be rapidly accreted by the planet to form its massive envelope. During this phase, Jupiter strongly perturbs near-by planetesimals, clearing a gap of increasing width in the planetesimals' disk. To model this second phase of Jupiter's formation we used a timescale derived from the hydrodynamical simulations described in Coradini et al. (2004): the value we employed in the simulation is $\tau_g = 5 \times 10^3$ years and is linked to the turbulence parameter $\alpha = 0.01$ employed in modeling the disc. During this phase, Jupiter's mass

growth is governed by the equation

$$(2) \quad M_p = M_c + (M_J - M_c) \times (1 - e^{(t - \tau_c)/\tau_g})$$

where $M_J = 1.8986 \times 10^{30} g = 317.83 M_{\oplus}$ is Jupiter's final mass.

In the third and final stage, Jupiter's accretion slows down while the giant planet reaches its final mass value and its gravitational perturbations start to secularly affect more and more distant planetesimals. While Jupiter's mass growth is still governed by eq.2 and there is no discontinuity from a numerical point of view between this phase and the previous one, we considered them as two separate stages of Jupiter's formation due to their different effects on the early Solar System, as we will describe broadly in section 3. We followed the evolution of the system across the second and third stages for $\tau_a = 7 \times 10^5$ years. Theoretical models indicate that forming giant planets go subject to external torques caused by the gravitational interaction between the planet and the protoplanetary disk: as a consequence of these torques, Jupiter is expected to radially migrate inward. To evaluate the effects of the radial displacement of the planet on the dynamical stability of the planetesimals' disk, in our simulations we forced Jupiter to migrate. Like the growth of the gaseous envelope, also the radial displacement starts at the beginning second phase of Jupiter's formation and reaches an asymptotic state in the third phase. The equation governing the radial migration is similar to eq. 2:

$$(3) \quad r_p = r_0 + (r_J - r_0) \times (1 - e^{(t - \tau_c)/\tau_r})$$

where r_0 is Jupiter's position at the beginning of the simulation (depending on the desired displacement), r_J is the final (present) position and $\tau_r = \tau_g = 5 \times 10^3$ years. In order to better evaluate the effects of migration, in our set of simulations we considered four different displacements: 0 AU (no migration), 0.25 AU, 0.5 AU and 1 AU. The initial semimajor axis of Jupiter has been consequently chosen so that its value at the end of the simulations would correspond to the one the planet possesses at present time.

2.2. Dynamical characterisation of the planetesimals. The initial distribution of the planetesimals in our simulations populated a region of phase space defined as follows:

$$(4) \quad \begin{aligned} 2 \text{ AU} &\leq a_i \leq 10 \text{ AU} \\ 0 &\leq e_i \leq 3 \times 10^{-2} \\ 0 \text{ rad} &\leq i_i \leq 10^{-2} \text{ rad} \end{aligned}$$

The values of eccentricity and inclination associated to each massless particle in our simulation have chosen randomly as

$$(5) \quad e_i = e_0 X$$

and

$$(6) \quad i_i = i_0 (1 - X)$$

where $e_0 = 10^{-2}$, $i_0 = 10^{-2} \text{ rad}$ and X is a random number extracted from a uniform distribution with $0 \leq X \leq 1$. The radial distribution of the planetesimals has been obtained by assuming the relationship between the mass and the heliocentric distance of the planetesimals described in Coradini et al. (1981) with superimposed a Maxwell-Boltzmann distribution. The number surface density in the planetesimals' disk can therefore be expressed as a function of mass and radial distance as

$$(7) \quad n(m, r) = Q(r) m^2 e^{-(m/\bar{m}_p(r))^2}$$

where $Q(r)$ represents the radial dependence of the number surface density $n(m, r)$ and, following Coradini et al. (1981), $\bar{m}_p(r)$ is the average mass of the planetesimals as a function of heliocentric distance given by the relationship

$$(8) \quad \bar{m}_p = m_0 \left(\frac{r}{1 \text{ AU}} \right)^\beta$$

where \bar{m}_p and m_0 are expressed in g , r is expressed in AU and $\beta = 1.68$. The value m_0 is the average mass of a planetesimal at 1 AU . The functional form of $Q(r)$ can be obtained by coupling eq. 7 with the relationship governing the surface density profile in the Solar Nebula

$$(9) \quad \sigma_p(r) = \alpha \sigma(r) = \alpha \sigma_0 \left(\frac{r}{1 \text{ AU}} \right)^{-n_s}$$

where we assumed the standard density-heliocentric distance relationship and put $n_s = 1.5$. The value σ_p is the mass density of the planetesimals, σ is the mass density of the gas in the Solar Nebula, σ_0 is the mass density of the gas at 1 AU and α is the dust to gas ratio: here we made the classical assumption $\alpha = 10^{-2}$. In the following, all the distances r , when normalised to 1 AU , will be indicated with the capital letter R while the symbol AU will indicate the value $1 \text{ AU} = 1.49597870691 \times 10^{13} \text{ cm}$.

By integrating eq. 7 over m we obtain

$$(10) \quad \begin{aligned} n^*(r) &= \int_0^\infty n(m, r) dm = \\ &= \int_0^\infty Q(r) m^2 e^{-(m/\bar{m}_p(r))^2} dm = \frac{\sqrt{\pi}}{4} Q(r) \bar{m}_p(r) \end{aligned}$$

while for the mass surface density of planetesimals we have

$$(11) \quad \sigma_p(r) = \int_0^\infty n(m, r) m dm = \int_0^\infty Q(r) m^3 e^{-(m/\bar{m}_p(r))^2} dm = \frac{1}{2} Q(r) \bar{m}_p^4(r)$$

By equating eq. 11 with eq. 9 we get

$$(12) \quad Q(r) = 2 \frac{\alpha \sigma_0}{\bar{m}_p^4} R^{-n_s}$$

which, substituting 12 into 10 and applying eq. 8, gives

$$(13) \quad n^*(r) = \frac{\sqrt{\pi}}{2} \frac{\alpha \sigma_0}{m_0} R^{-(n_s + \beta)}$$

Now we can obtain the cumulative distribution of $n^*(r)$ by integrating

$$(14) \quad N(x) = \int_{r_{min}}^x 2\pi r n^*(r) dr \\ = \pi^{3/2} \frac{\alpha \sigma_0}{m_0} (AU)^2 \left(\frac{1}{2 - n_s - \beta} \right) \left(\left(\frac{x}{AU} \right)^{2-n_s-\beta} - \left(\frac{r_{min}}{AU} \right)^{2-n_s-\beta} \right)$$

where $r_{min} = 2 AU$ is the inner radius of the planetesimals' disk. We can obtain the total number of planetesimals in the disk by integrating eq. 14 between $r_{min} = 2 AU$ and $r_{max} = 10 AU$:

$$(15) \quad N_{tot} = \int_{r_{min}}^{r_{max}} 2\pi r n^*(r) dr = \\ = \pi^{3/2} \frac{\alpha \sigma_0}{m_0} (AU)^2 \left(\frac{1}{2 - n_s - \beta} \right) \left(\left(\frac{r_{max}}{AU} \right)^{2-n_s-\beta} - \left(\frac{r_{min}}{AU} \right)^{2-n_s-\beta} \right)$$

The function $X = \frac{N(x)}{N_{tot}}$ uniformly varies in the range $0 \leq X \leq 1$. Once we invert previous equation and express the initial position of the planetesimals in the disk as $x = f(X)$ where

$$(16) \quad x = f(X) = \left[X \left(\left(\frac{r_{max}}{AU} \right)^{2-n_s-\beta} - \left(\frac{r_{min}}{AU} \right)^{2-n_s-\beta} \right) + \left(\frac{r_{max}}{AU} \right)^{2-n_s-\beta} \right]^{n_s+\beta-2}$$

we can use X as the random variable in a Montecarlo extraction to spatially populate the disk. Through eq. 8 we can link the average mass $\bar{m}_p(r)$ of the planetesimals to their initial position $r = x$ (which we assume coinciding with the formation region). To obtain each planetesimal's mass value, we apply again a Montecarlo method through a uniform random variable Y . To obtain Y we need to compute and normalise the cumulative distribution of eq. 7 considering m as the variable of interest and r as a constant. The cumulative distribution is

$$(17) \quad \int_0^{m^*} n(m, r) dm = \frac{2\alpha\sigma_0}{\bar{m}_p(r)} R^{-n_s} \int_0^{y^*} y^2 e^{-y^2} dy$$

where $y = m/\bar{m}_p(r)$ and $y^* = m^*/\bar{m}_p(r)$.

The integral in the right side of eq. 17 cannot be solved analytically: substituting $z = y^2$ with $dz = 2ydy$ we obtain

$$(18) \quad \int_0^{y^*} y^2 e^{-y^2} dy = \frac{1}{2} \int_0^{\sqrt{z^*}} z^{1/2} e^{-z} dz$$

The integral on the right side of previous equation is a lower incomplete Gamma function with real parameter $a = 3/2$ or $\gamma(3/2, \sqrt{z^*})$. Normalising eq. 17 over eq. 13 we get the uniform random variable Y varying in the range $[0, 1]$

$$(19) \quad Y = \frac{2\gamma(3/2, y^*)}{\sqrt{\pi}} = P(3/2, y^*)$$

where $P(3/2, y^*)$ is the lower incomplete Gamma ratio. The inverse of the lower incomplete Gamma ratio can be computed numerically and, by substituting y^* back with $m^*/\bar{m}_p(r)$ we obtain

$$(20) \quad m(r) = \bar{m}_p \text{inv}(P(3/2, Y))$$

We can therefore assign to each planetesimal its own mass value through a second Montecarlo extraction.

The number of massless particles we used in our simulations has been $n_{mp} = 8 \times 10^4$ to optimise the computational load. The use of massless particles assures the linearity of the processes over the number of considered bodies: we can therefore extrapolate the number of impacts expected in a disk of planetesimals described by the density profiles previously presented by multiplying the number of impacts recorded in our simulations by a factor γ where

$$(21) \quad \gamma = N_{tot}/n_{mp}$$

where N_{tot} is computed through eq. 15. The γ factor is independent from heliocentric distance r since the n_{mp} planetesimals have been distributed following the number density profile $n^*(r)$ of the disk.

The dynamical evolution of Jupiter and the swarm of massless particles is computed through a fourth order Runge-Kutta integrator with a self adjusting time-step. To choose the time-step, our numerical code evaluates the smallest timescale in the simulations at a given time between:

- the orbital periods of the massless particles
- the orbital periods of Jupiter and the two asteroids
- the free-fall timescale of each pair massless particle-Jupiter considered as an isolated system

The time-step employed is computed by the code as

$$(22) \quad t_{ts} = \tau_{min}/f_{ts}$$

where $f_{ts} = 100$ in our simulations.

2.3. Chemical and physical characterisation of planetesimals. To evaluate the possible amount of volatiles delivered to the asteroids from the planetesimals, we recorded the initial positions of the massless particles in our simulations. We assumed that the initial positions of the particles coincided with their formation regions. We considered two compositional classes:

- particles formed inside the Snow Line (**ISL** in the following) were considered rocky bodies
- particles formed beyond the Snow Line (**BSL** in the following) were considered icy bodies

ISL and BSL particles were characterised by mean density values respectively $\rho_{ISL} = 3.0 \text{ g/cm}^3$ and $\rho_{BSL} = 1.0 \text{ g/cm}^3$. The location of the Snow Line in our simulations has been fixed at $r_{SL} = 4.0 \text{ AU}$ (see Encrenaz (2008) and references therein).

2.4. Collisional history. To reproduce the collisional histories of the two asteroids, instead to follow the explicit dynamics of Vesta and Ceres and proceed in a deterministic way, we opted for a statistical approach. Each asteroid was spread into a torus with mean radius R_T and section σ_T defined as

$$(23) \quad R_T = a_A$$

and

$$(24) \quad \sigma_T = \frac{\pi}{4} \times (D_A f_G)^2$$

where a_A and D_A were respectively the semimajor axis and the physical diameter of the considered asteroid while f_G is the gravitational focusing factor

$$(25) \quad f_G = 1 + \left(\frac{v_{esc}}{v_{enc}} \right)^2$$

with v_{esc} being the escape velocity from the asteroid and v_{enc} being the relative velocity between the asteroid and the impacting planetesimal. The gravitational focussing factor f_G was introduced to account for the perturbations produced by the asteroid on the orbits of the planetesimals, which were not included in the explicit dynamical model.

When a planetesimal crosses one of the asteroids' torii, the impact probability is the probability that both planetesimal and asteroid will occupy the same region at the same time. This probability can be evaluated as the ratio between the *effective collisional time* and the orbital period of the asteroid. The effective collisional time is the amount of time available for collisions and is evaluated as the minimum between

the time spent by the asteroid and the planetesimal into the crossed region of the torus. This is equivalent to writing

$$(26) \quad P_{coll} = \frac{\min(\tau_P, \tau_A)}{T_A}$$

where T_A is the orbital period of the asteroid, τ_A is the time spent by the asteroid into the crossed region, τ_P is the time spent by the planetesimal into the torus and $\min(\tau_P, \tau_A)$ is the effective collisional time.

To estimate τ_P and τ_A we need to identify the intersections of the planetesimals' orbits with the asteroids' torii. Our approach is based on a linearisation of the problem, i.e. we approximated with a line the orbital path of the planetesimal while passing near a torus and solved the ray-torus intersection problem. A torus centred on the origin of the axes and lying on the xy plane is described by the equation

$$(27) \quad f(x, y, z) = (x^2 + y^2 + z^2 - (R^2 + s^2)) + 4R^2(z^2 - s^2)$$

where $R = R_T$ and $s = 0.5(D_A f_G)$. The surface of the torus is described by the homogeneous equation $f(x, y, z) = 0$: by substituting the variables (x, y, z) with the vectorial equation of the ray associated to the linearised orbit

$$(28) \quad \vec{r} = \vec{m}t + \vec{q}$$

where m and q are respectively the angular coefficient and the origin of the ray, we obtain the fourth order equation identifying the intersections between the ray and the torus. By writing

$$(29) \quad a = \vec{m} \cdot \vec{m}$$

$$(30) \quad b = \vec{m} \cdot \vec{q}$$

$$(31) \quad c = \vec{q} \cdot \vec{q}$$

we can express the fourth order equation as

$$(32) \quad d_4t^4 + d_3t^3 + d_2t^2 + d_1t^1 + d_0 = 0$$

where

$$(33) \quad \begin{aligned} d_4 &= a^2 \\ d_3 &= 4ab \\ d_2 &= 4b^2 - 2as^2 - 2aR^2 + 2ac + 4R^2m_z^2 \\ d_1 &= 4bc - 4bs^2 - 4bR^2 + 8m_zq_zR^2 \\ d_0 &= c^2 + R^4 + s^4 - 2R^2s^2 - 2cs^2 - 2cR^2 + 4R^2q_z^2. \end{aligned}$$

This fourth order equation can be solved analytically through Ferrari's method. The quartic equation will have up to four real solutions, depending on the number of intersections: by selecting the appropriate pair of real solutions, if existing, we can derive the coordinates of the intersection points \vec{x}_1 and \vec{x}_2 . From the intersection points we can derive the length of the planetesimal's path d_P through the torus and the crossing time τ_P which, in the linear approximation, is

$$(34) \quad \tau_P = \frac{d_P}{|\vec{v}_P|}$$

where $|\vec{v}_P|$ is the modulus of the velocity of the planetesimal.

From the knowledge of the intersection points we can also derive the angular width of the crossed section of the torus $\Delta\theta_A$ and the time τ_A the asteroid spends into the crossed region:

$$(35) \quad \tau_A = \Delta\theta_A \frac{T_A}{2\pi} = \frac{\Delta\theta_A}{\omega_A}$$

where $\omega_A = n_A = \frac{2\pi}{T_A}$ is the angular velocity (coinciding with the orbital mean motion for circular orbits) of the asteroid.

2.5. Impact cratering. To evaluate the effects of the impacts on the surface cratering of the two asteroids, for each recorded collision we computed the average crater diameter using the empirical scaling law (see p. 165 of De Pater & Lissauer (2001))

$$(36) \quad D = 1.8 \rho_i^{0.11} \rho_a^{1/3} (2R_i)^{0.13} \left(\frac{E_k}{g_a} \right)^{0.22} (\sin\theta)^{1/3}$$

where the letters a and i indicate the asteroid and the impactor respectively, ρ is the density, R the physical radius, g the gravitational acceleration, E_k is the impact kinetic energy and θ is the impact angle respect to the local horizontal. In our estimation of the surface cratering we used a fixes value $\theta = 45^\circ$ as the average impact angle (see Pierazzo & Melosh (2000) and references therein).

2.6. Parallelising the model. Before concluding the section devoted to the dynamical and physical model, we would like to emphasize one advantage of our modelization, i.e. the possibility to parallelise the evolution of the template of the Solar System in a straightforward way. Since the disc of planetesimal is composed only of massless particles, which by definition do not interact between themselves, and since Jupiter's evolution is driven by the migration and accretions rates described by eqs. 1, 2 and 3, we are able to split each simulation into a set of sub-problems which can be treated in parallel. In our implementation, we used a GRID-like approach by dividing the disc of planetesimals into a number of concentric rings containing a fixed amount of test particles. Each ring has been evolved independently under the

influence of the forming Jupiter and the collisions with the two asteroids recorded. At the end of the simulations, by merging the results we obtained a representation of the evolution of the system as a whole. Obviously, a different normalisation factor has to be used for each ring of massless particles to normalise it to the real population expected in the orbital region considered. Through this approach, we have been able to run the equivalent of a 3-month long simulation with 8×10^4 massless particles by running a set of 8 sub-simulations with 10^4 massless particles each, every sub-simulation taking about 12 days to conclude.

3. RESULTS

In our simulations we identified 4 distinct dynamical families contributing to the cratering of Vesta and Ceres in the temporal framework considered. Two of these families (a resonant and a non-resonant one) belonged to the ISL population and two (again, a resonant and a non-resonant one) to the BSL population.

3.1. Dynamical features of the impactors. The ISL impactors can be divided into two main dynamical groups (see figs. 1 and 2). The first one is composed by bodies orbitally near the two asteroids and represents the population of bodies contributing to the accretion process of the asteroids, hereafter indicated as *primordial impactors*. For this population collisions start shortly after the beginning of the simulations and would deplete the population if not for the dynamical perturbations of Jupiter, which inject new massless particles on Vesta-crossing or Ceres-crossing orbits. The second ISL group is composed of families of *resonant impactors*, with the number of active resonances and their relative abundances of impactors strongly depending on the extent of Jupiter's displacement. As a rule of the thumb, the resonance affecting each asteroid for all cases considered of Jupiter's migration is the one located nearest to the respective orbital regions. The flux of impactors due to the resonances increases with increasing displacements of Jupiter (see figs. 1 and 2), as is to be expected since the resonances co-move inward with the giant planet and sweep larger orbital regions, affecting more massless particles. The resonances affecting Vesta and Ceres in the temporal framework of our simulations are located at about 2.5 AU and 3.5 AU (see figs. 1 and 2): they appear in the simulations after the beginning of the rapid gas accretion phase, when Jupiter's mass is high enough to strongly excite the resonances. Ceres' resonant impactors (fig. 2) have eccentricities distributed between $0.1 - 0.2$ if originating from the 2.5 AU region and $0.1 - 0.6$ if originating from the 3.5 AU region. The eccentricity values of Vesta's resonant impactors (fig. 1) are distributed in the range $0.05 - 0.2$ for objects coming from the 2.5 AU region and $0.2 - 0.5$ for those coming from the 3.5 AU region.

Also between the BSL impactors we detected two dynamical groups (see figs. 1 and 2): a first, sparse one composed of non-resonant bodies scattered by Jupiter's

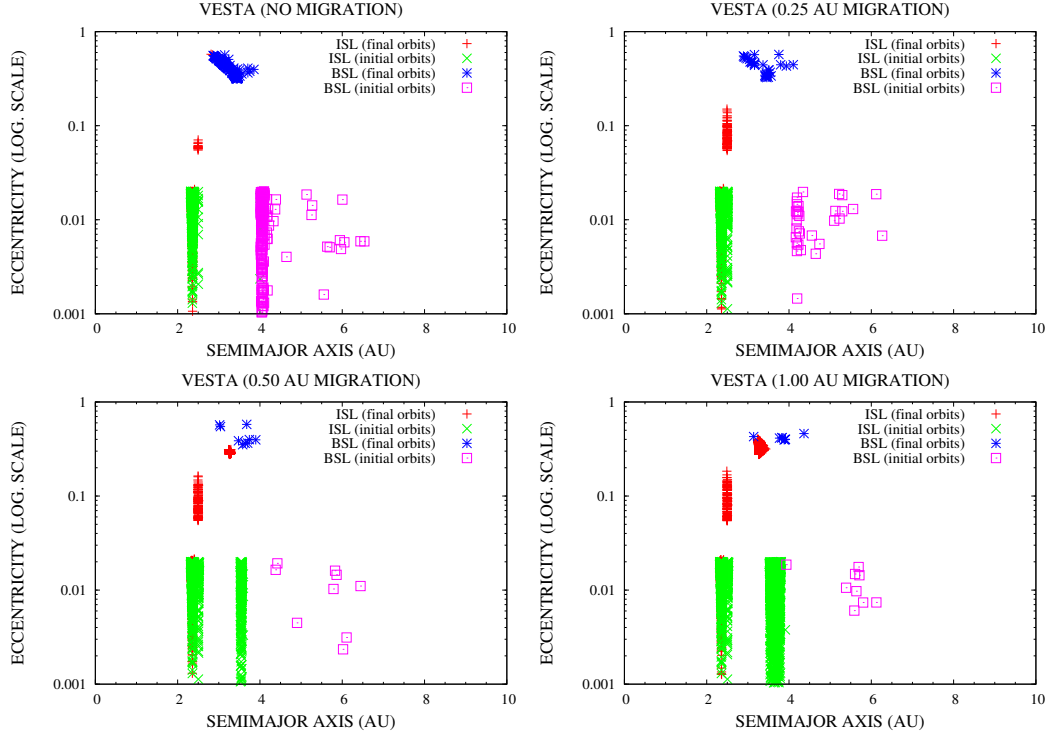


FIGURE 1. Semilogarithmic plots of the orbital elements of Vesta's impactors in the $a - e$ plane. Red and green symbols represent respectively the final (at impact) and initial orbits of ISL impactors, while the blue and magenta symbols represent respectively the final and initial orbits of BSL impactors. As is clearly visible from the plots, ISL impactors are divided in two dynamical families, a first, primordial one and a second, resonant one (see section 3.1 for details). Also the BSL impactors can be divided between non-resonant and resonant bodies, but the latters disappear for increasing values of Jupiter's radial displacement (0.5 and 1 AU). Note that these plots show only the dynamical classes of impactors recorded in the simulations since they are not normalised to the real disc population.

gravitational perturbations and a second, narrower one (located near the Snow Line) related to a mean motion resonance with the giant planet. Non-resonant planetesimals are dynamically destabilised when Jupiter's mass reaches a significant fraction of its final value and part of them is injected into the inner Solar System on Ceres-crossing and Vesta-crossing orbits. The existence and the abundance of the BSL resonant population are strictly linked to the extent of Jupiter's radial displacement,

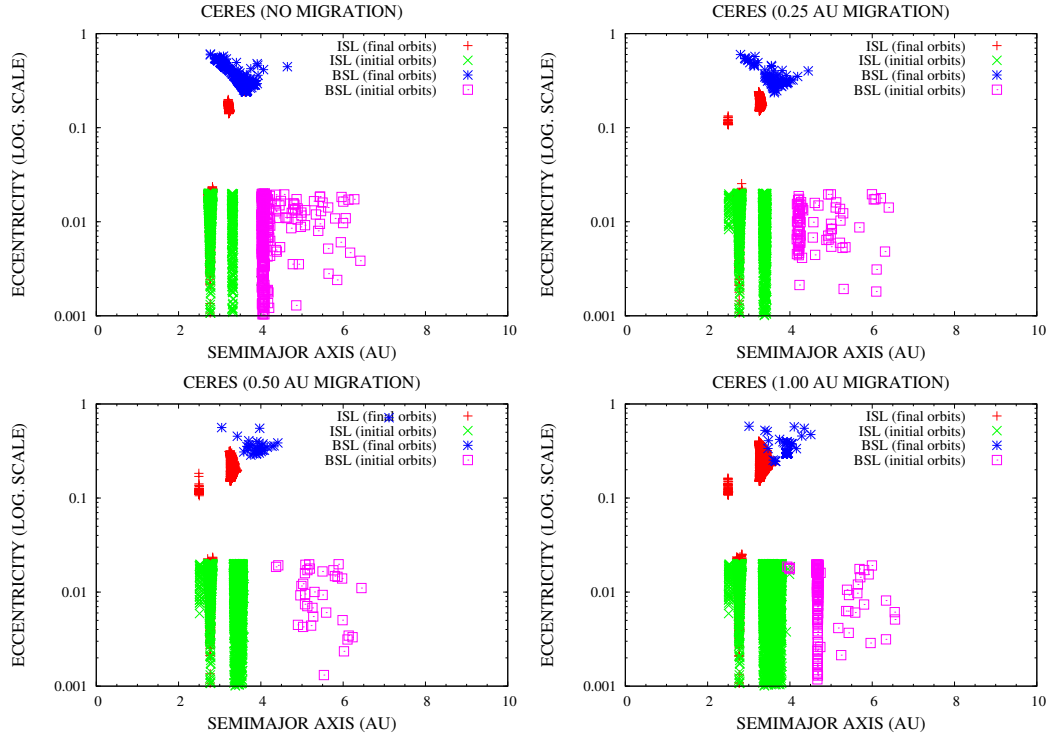


FIGURE 2. Semilogarithmic plot of the orbital elements of Ceres' impactors in the $a-e$ plane. Red and green symbols represent respectively the final (at impact) and initial orbits of ISL impactors, while the blue and magenta symbols represent respectively the final and initial orbits of BSL impactors. As in fig. 1, both ISL and BSL impactors can be divided into a non-resonant and a resonant population. In Ceres' case, however, the resonant BSL population is present in three of our dynamical scenarios (i.e. it doesn't appear in the case of Jupiter's 0.5 AU radial displacement). Note that these plots show only the dynamical classes of impactors recorded in the simulations since they are not normalised to the real disc population.

both for Vesta and Ceres. Increasing values of the radial displacement cause a decrease in the number of resonant BSL impactors. However, in Ceres' case, a new resonant population originating near 4.6 AU appears in the 1 AU migration scenario. The final orbits of all BSL impactors are characterised by high eccentricity values, in the range $0.3 - 0.7$ for Vesta (fig. 1) and $0.2 - 0.6$ for Ceres (fig. 2).

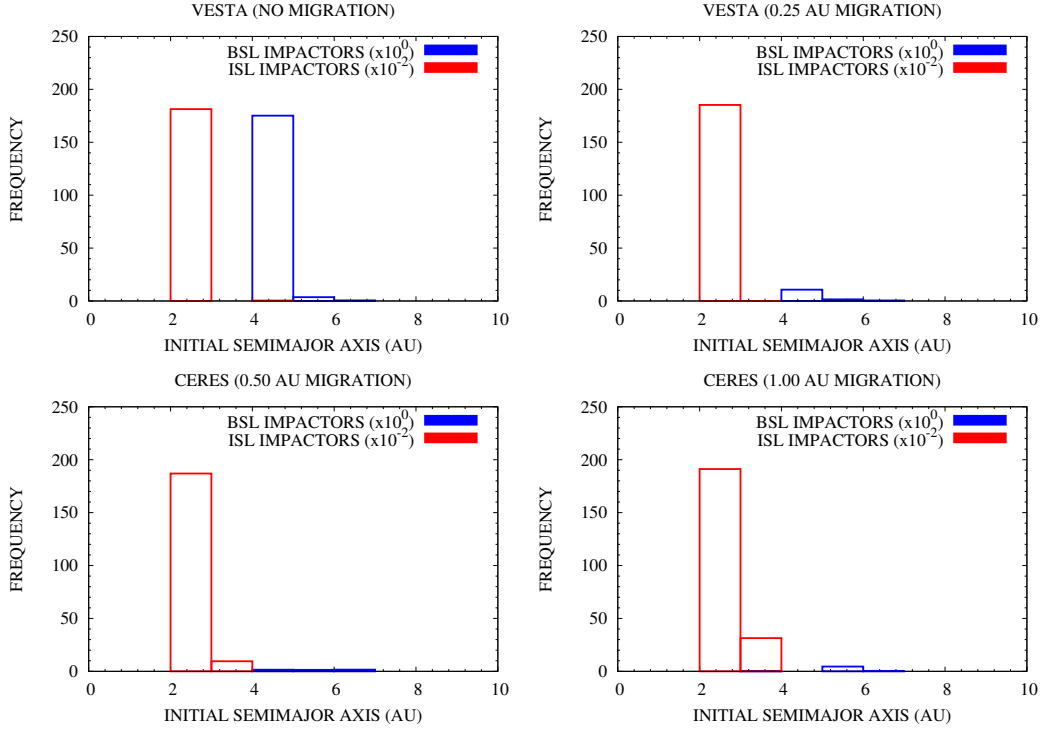


FIGURE 3. Frequency versus formation region histograms of Vesta’s impactors normalised over the real planetesimal population: red bars are those related to ISL impactors, blue ones to BSL impactors. The frequency of ISL impactors in all plots has been divided by a factor 100 to enhance the readability and facilitate the comparison of the plots. Once normalised, ISL planetesimals completely dominate the flux of impactors on Vesta. The peak in BSL impactors in the top left plot is due to the excitation of an orbital resonance with Jupiter.

3.2. Characterization of the flux of impactors. The dynamical classes of impactors we showed in figs. 1 and 2 and discussed in previous section represent the events recorded during our simulations and are not representative of the real flux of impactors. In figs. 3 and 4 we show the normalised frequency versus formation region distributions of both ISL and BSL impactors in all the migration scenario we considered. As is clearly visible, ISL impactors are 2 – 3 orders of magnitude more abundant than BSL impactors and completely dominate the craterisation histories of the two asteroids. The frequency of BSL impactors is greatly enhanced in those migration scenarios where Jupiter excites resonances in the orbital region outside the

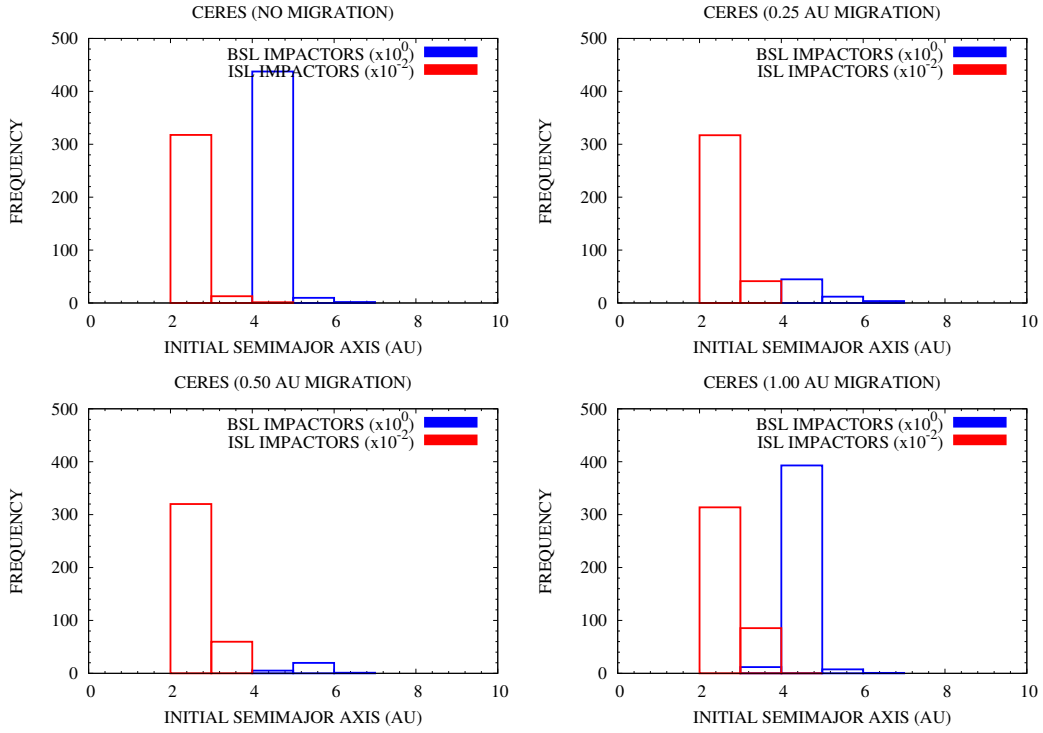


FIGURE 4. Frequency versus formation region histograms of Ceres's impactors normalised over the real planetesimal population: red bars are those related to ISL impactors, blue ones to BSL impactors. The frequency of ISL impactors in all plots has been divided by a factor 100 to enhance the readability and facilitate the comparison of the plots. The flux of BSL impactors, while by far inferior than that of ISL bodies, is significantly higher than in the case of Vesta. The peaks in BSL impactors in the top left and bottom right plots are due to the excitation of different orbital resonances with Jupiter, while the importance of the analogue resonance in the 0.25 AU migration scenario is greatly reduced after the normalisation.

Snow Line, as we mentioned in previous section.

3.2.1. *ISL impactors.* The flux of ISL impactors on the two asteroids is characterised by two phases (see figs. 5 and 6). The first phase covers the time it takes the planet to form a critical mass core and accrete a significant mass of gas: during this phase the flux of impactors on the asteroids is dominated by primordial impactors. The

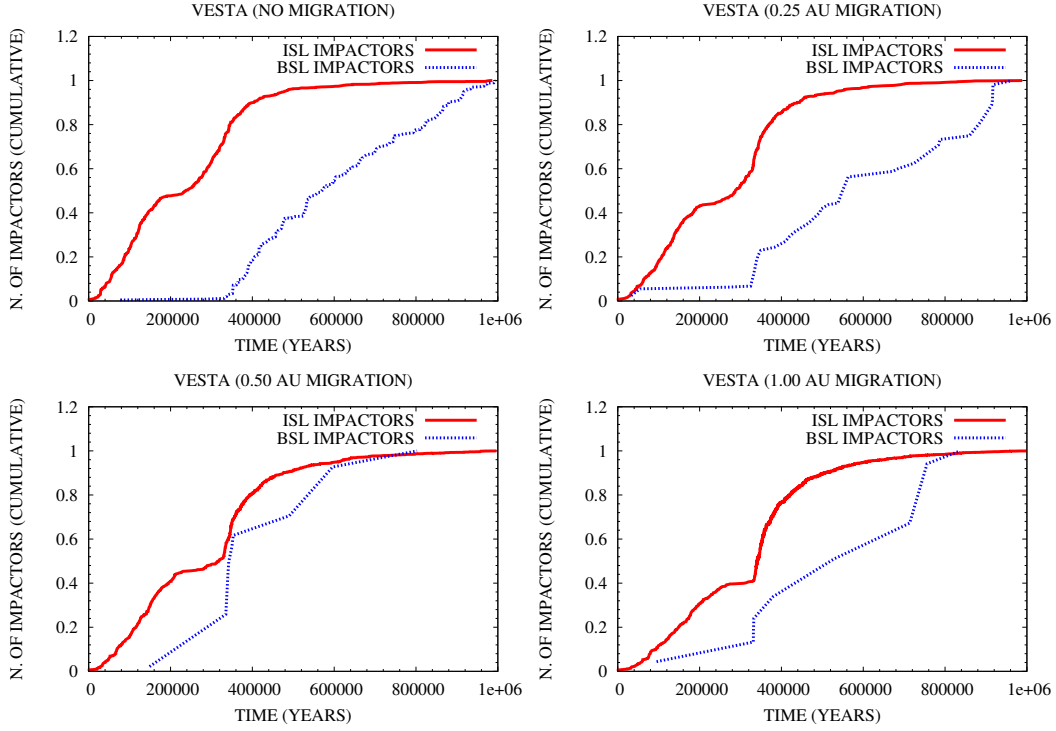


FIGURE 5. Normalised cumulative distribution of the flux of impactors over time for Vesta: the red curve is related to ISL impactors, the blue one to BSL impactors. In all plots the fluxes have been normalised to their values at the end of the simulations. The flux of ISL impactors is divided into two main phases: a first one due to the contribution of primordial impactors and a second one, starting after Jupiter accretes a significant mass, due to both primordial and resonant impactors. In both phases, the growth of the cumulative flux slows down with time and eventually stops. The flux of BSL impactors begin when Jupiter's gaseous envelope reaches a significant mass and the cumulative distribution grows until the end of the simulations.

steepness of the cumulative flux during this phase varies depending on Jupiter's location: the farther Jupiter formed from its present orbit, the lesser the steepness of the curve (see figs. 5 and 6). This can be intuitively explained by Jupiter being less effective at injecting new primordial impactors on Vesta-crossing or Ceres-crossing orbits when it forms farther from their location. In the last third of the first phase, between 2×10^5 and 3×10^5 years, the flux of ISL primordial impactors stops both in Vesta's and Ceres' cases (see figs. 5 and 6). The length of the stop in the flux of

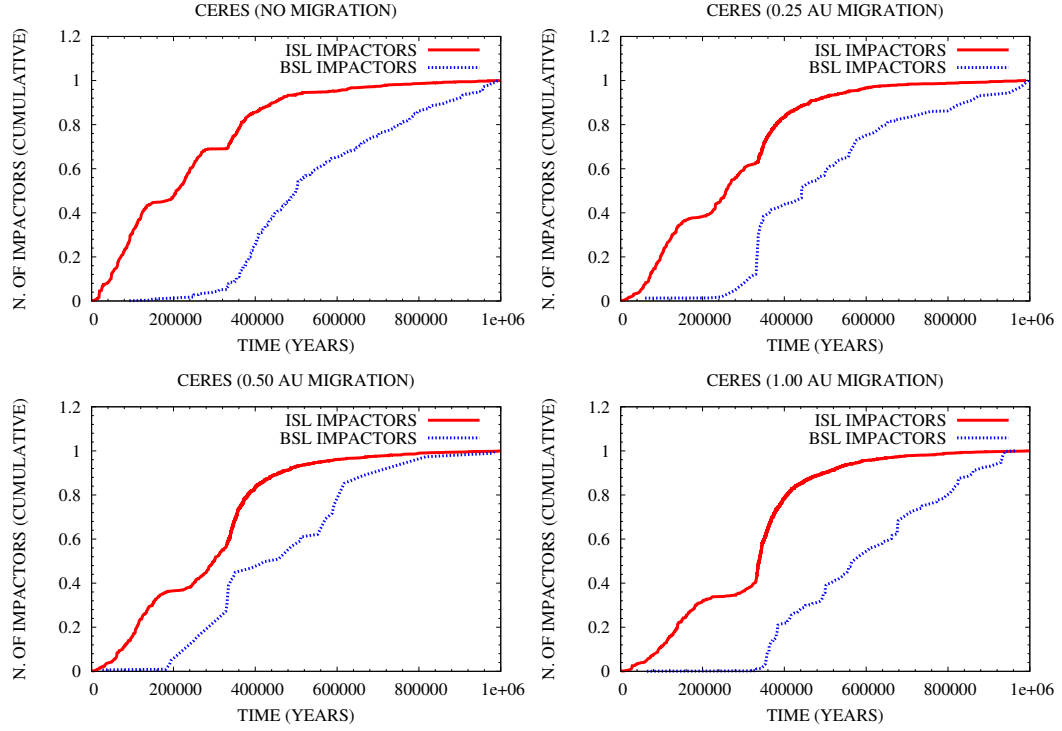


FIGURE 6. Normalised cumulative distribution of the flux of impactors over time for Ceres: the red curve is related to ISL impactors, the blue one to BSL impactors. In all plots the fluxes have been normalised to their values at the end of the simulations. Most of the considerations exposed for Vesta's case (see fig. 5) are valid also for Ceres. The transition between the two phases for ISL impactors mentioned in fig. 5 is clearly dependent from Jupiter's formation region. For Jupiter forming near its final semimajor axis (0 and 0.25 AU cases), the gravitational perturbations of the growing core can affect the ISL planetesimals and cause a visible enhancement in the flux of impactors. If Jupiter formed farther (0.5 and 1 AU cases) the transition between the two phases is more clean.

impactors depends on the initial position of Jupiter (see figs. 5 and 6). If Jupiter formed nearer to the asteroids, as in the 0 and 0.25 AU migration scenarios, the core would start to inject new bodies on asteroid-crossing orbits once it approaches the critical mass. The influence of Jupiter's core then results in a smoother transition between the first and the second phase. If Jupiter formed farther away, as in the 0.5 and 1 AU migration scenarios, the core is unable to accomplish the same task and

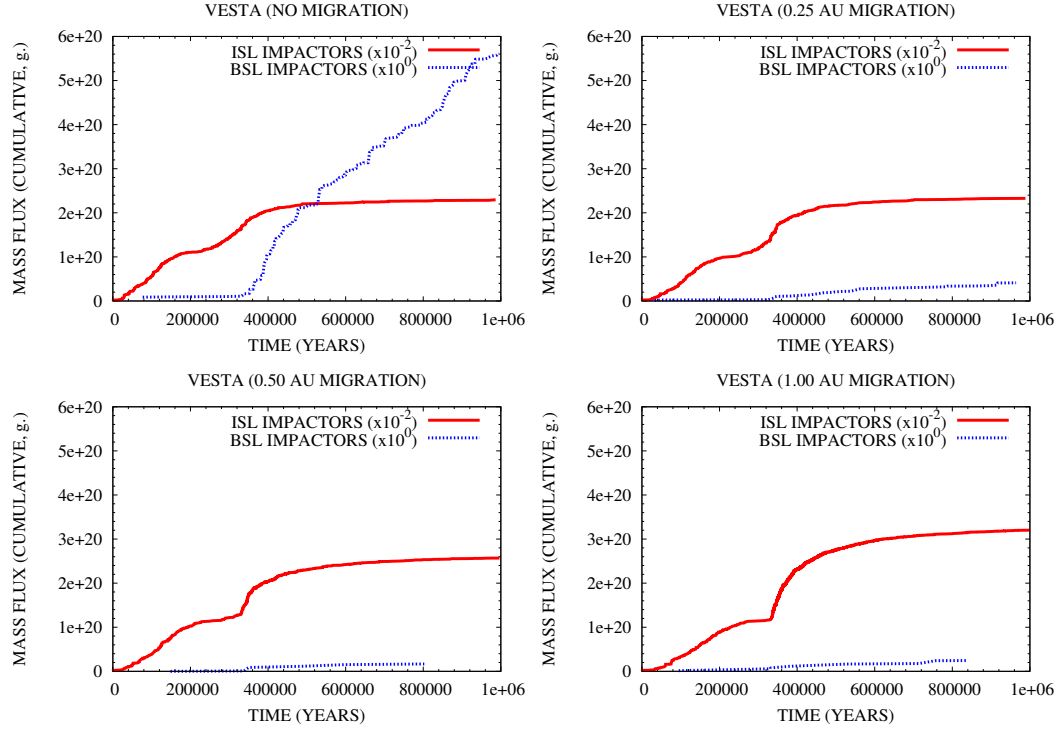


FIGURE 7. Cumulative distribution of the mass flux over time for Vesta: the red curve is related to ISL impactors, the blue one to BSL impactors. The mass flux of ISL impactors in all plots has been divided by a factor 100 to enhance the readability and facilitate the comparison of the plots. The overall features of the cumulative distribution of the mass flux are similar to those of the cumulative distribution of the flux of impactors (see fig. 5 for details).

the stop lasts till the beginning of the second phase, resulting in a more abrupt transition. The second phase starts when Jupiter is massive enough to significantly perturb the orbital resonances (see figs. 5 and 6). The flux of ISL impactors greatly increases on timescales of the order of that of Jupiter's mass growth, almost doubling in about $2 - 3 \times 10^4$ years. The flux then slows down as Jupiter clears the reservoir of planetesimals located near the mean motion resonances and bodies farther away are perturbed on longer timescales. During this second phase, the flux of ISL impactor is still sensitive to Jupiter's migration. This dependence can be seen from figs. 7 and 8: the figures show the cumulative mass fluxes on Vesta and Ceres respectively and the final values of the mass flux increase linearly with Jupiter's radial displacement. Finally, even if similar when normalised (see the captions of figs. 5 and 6 for details),

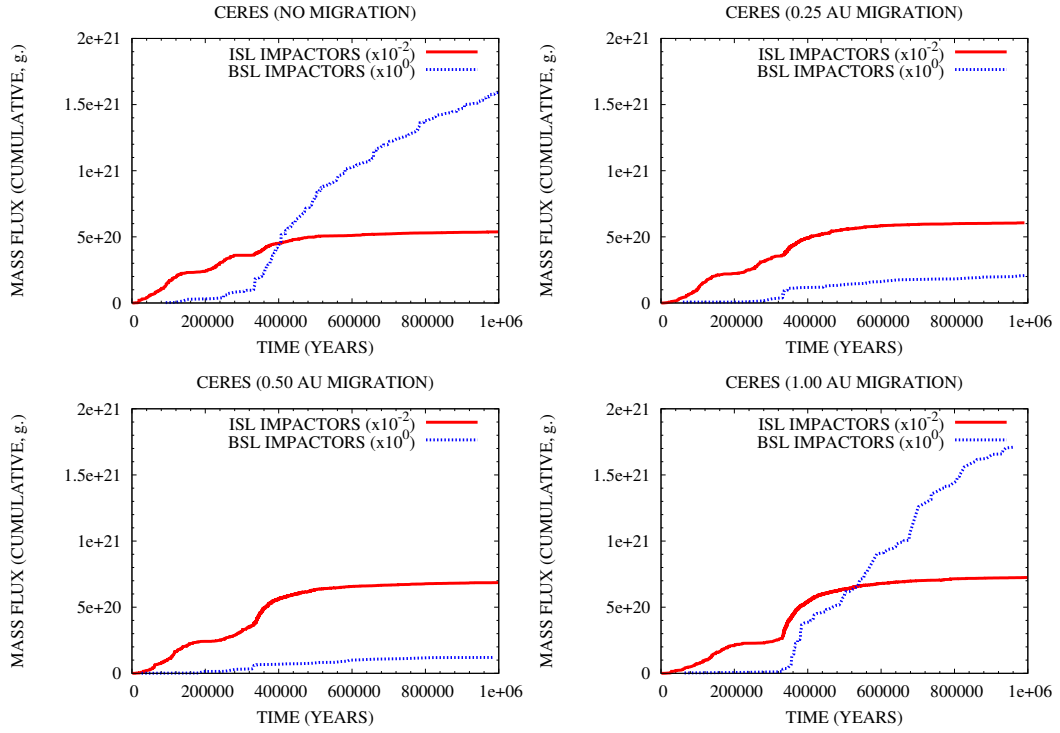


FIGURE 8. Cumulative distribution of the mass flux over time for Ceres: the red curve is related to ISL impactors, the blue one to BSL impactors. The number of ISL impactors in all plots has been divided by a factor 100 to enhance the readability and facilitate the comparison of the plots. The overall features of the cumulative distribution of the mass flux are similar to those of the cumulative distribution of the flux of impactors (see fig. 6 for details).

the flux of impactors (both primordial and resonant) on Vesta is about half than the corresponding one on Ceres (see figs. 7 and 8). This is due to the inner position of the former asteroid, which imposes stricter constrains on the dynamical evolution of the planetesimals to be injected on Vesta-crossing orbits.

3.2.2. BSL impactors. The flux of BSL impactors greatly varies depending on the considered asteroid and migration scenario. For Vesta, the only relevant contribution of BSL impactors to the cratering history of the asteroid appears in the 0 AU, no-migration scenario (see fig. 3). In this scenario, Vesta is hit by about 2×10^2 impactors (see fig. 3) once the flux is normalised on the real population of the disk of planetesimals. In all the other scenarios, the contribution of BSL impactors

is of the order of 10 events (see fig. 3). This implies that the expected flux of volatile-rich bodies on Vesta at the time of Jupiter's formation is about 3 orders of magnitude lower than that of rocky bodies, with the only exception being the case where Jupiter formed at its present location. Due to the mass-heliocentric distance relationship assumed in eq. 8, the mass of the planetesimals in the disc increases with the heliocentric distance. Once this effect is taken into account, in the no-migration scenario the mass flux of BSL planetesimals is about a factor 40 lower than the one of ISL planetesimals (see fig. 7). In all other three migration scenario, the ratio between the mass fluxes of ISL and BSL planetesimals doesn't change significantly (see fig. 7).

Ceres' case is analogous to Vesta's one, but the BSL flux of impactors is enhanced in the 0 AU and in the 1 AU cases due to the excitation of mean motion resonances. The enhancement results in overall fluxes 1 order of magnitude and mass fluxes 2 orders of magnitude greater than in the 0.25 AU and the 0.5 AU cases (see figs. 4 and 8). The enhanced fluxes and mass fluxes of BSL impactors are about a factor 3 higher than in Vesta's enhanced case (0 AU). In the non-enhanced cases (i.e. 0.25 AU and 0.5 AU) the mass fluxes of BSL impactors on Ceres are about an order of magnitude higher than the ones in Vesta's non-enhanced cases (see figs. 7 and 8).

The overall delivery of volatile-rich material in the orbital region of Ceres remains more than one order of magnitude lower than that of rocky material. We must note, however, that the injection of BSL planetesimals on asteroid-crossing orbits, being a secular process, didn't stop before the end of the simulations (see the trend of the BSL curves in figs. 5 and 6). The secular perturbations of Jupiter (and, in the real Solar System, of the other giant planets) could inject more bodies on asteroid-crossing orbits on timescales longer than the one covered by our simulations.

3.3. Characterization of the impacts. In our simulations we recorded the characteristics of each occurred impact detailing them by their dynamical features and their effects on the target (i.e. crater size and energy delivered to the asteroid). In the following we will describe our results.

3.3.1. Dynamical features. While considering the dynamical features, we observe three classes of impacts which are common both to Vesta's and Ceres' impactors. The first class is composed by the ISL primordial impactors: is characterised by low impact velocities, always inferior to 1 km/s , and a continuous mass spectrum over the range we considered (see figs. 9 and 10). The second class is composed by the ISL resonant impactors: this class too has a continuous mass spectrum, but the characteristic velocities are systematically higher than those of the first class, ranging between $1 - 10 \text{ km/s}$ (see figs. 9 and 10). The third class of impacts is due to the BSL impactors: there is no evident distinction between the impacts due to BSL resonant and non-resonant planetesimals, with the only exception of the Ceres' 1 AU

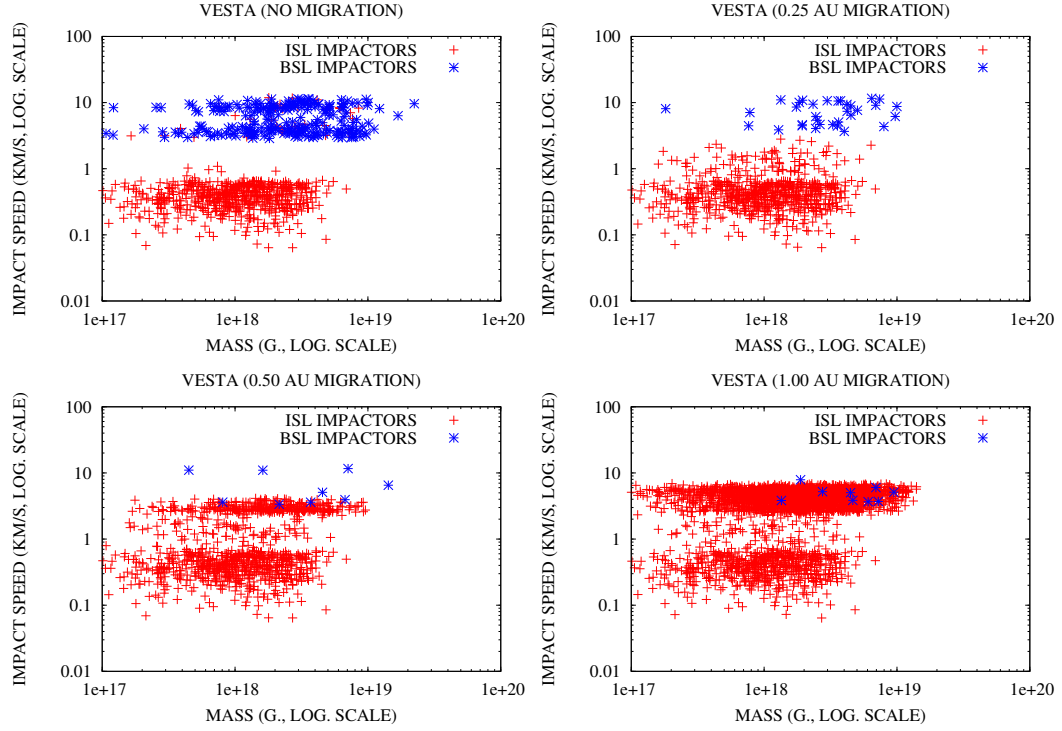


FIGURE 9. Dynamical characterisation of the impacts on Vesta: red symbols indicated ISL impactors and blue ones BSL impactors. The data reproduced in the plots are the events recorded in our simulations: they have not been normalised to the real population of the planetesimal disc and are used only to show the observed dynamical classes. As can be seen from the plots, ISL resonant and primordial impactors are characterised by different dynamical features, while no difference is evident between resonant and non-resonant BSL impactors in those scenario with Jupiter migrating. In the no-migration scenario BSL impactors seem to divide in two clusters, a first between $3 - 4 \text{ km/s}$ and a second between $8 - 10 \text{ km/s}$. The relative abundance of bodies in the two clusters, however, argues against attributing this effect to the non-resonant versus resonant subdivision (see fig. 1).

migration scenario. The BSL impactors globally tend to cluster towards higher mass values as a consequence of the mass-heliocentric distance relationship assumed in the model (eq. 8). The impact speeds of BSL impactors mostly overlap the same range of values of the resonant ISL impactors but, depending on the migration scenario, a fraction can hit the asteroids with velocities higher than 10 km/s (see figs. 9 and

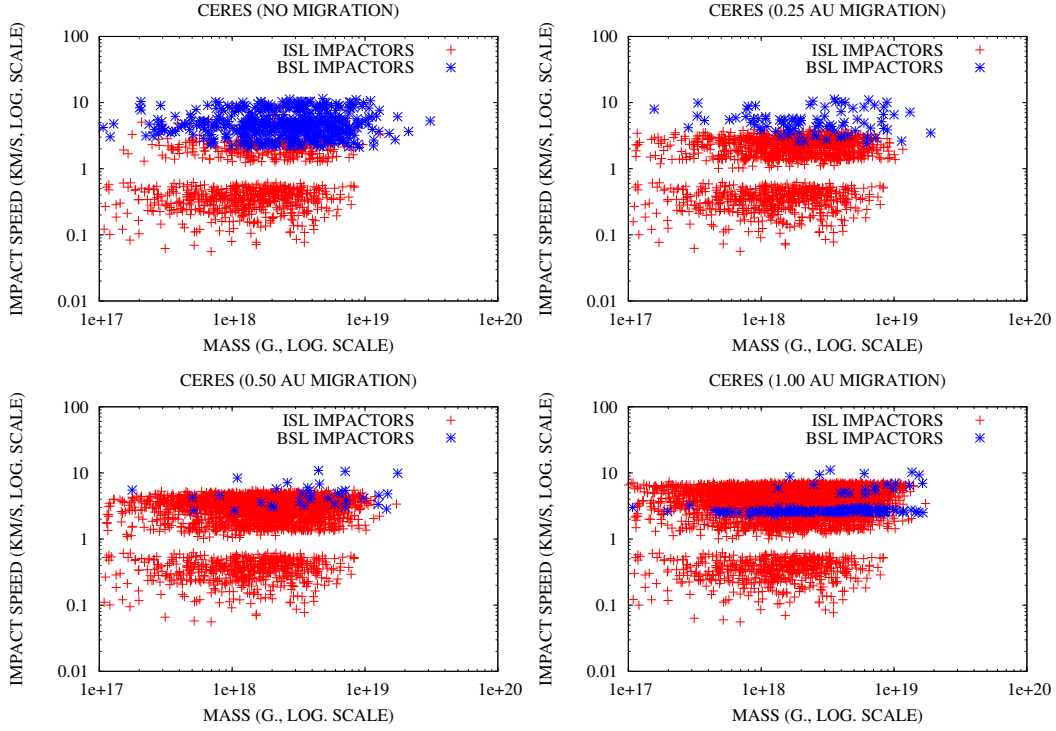


FIGURE 10. Dynamical characterisation of the impacts on Ceres: red symbols indicated ISL impactors and blue ones BSL impactors. The data reproduced in the plots are the events recorded in our simulations: they have not been normalised to the real population of the planetesimal disc and are used only to show the observed dynamical classes. As can be seen from the plots, ISL resonant and primordial impactors are characterised by different dynamical features, while no difference is evident between BSL resonant and non-resonant impactors in the first three migration scenarios. In the 1 AU migration scenario, resonant BSL impactors cluster in the range 2–3 km/s while non-resonant BSL impactors are characterised by higher velocities.

10). In one case we recorded an impact velocity value of about 20 km/s (see fig. 10, bottom right panel).

3.3.2. Impact craters. While considering the craterisation due to the impacts, we observe that ISL and BSL planetesimals form two different classes. As a general rule, ISL-related craters completely dominate the crater distributions on the two

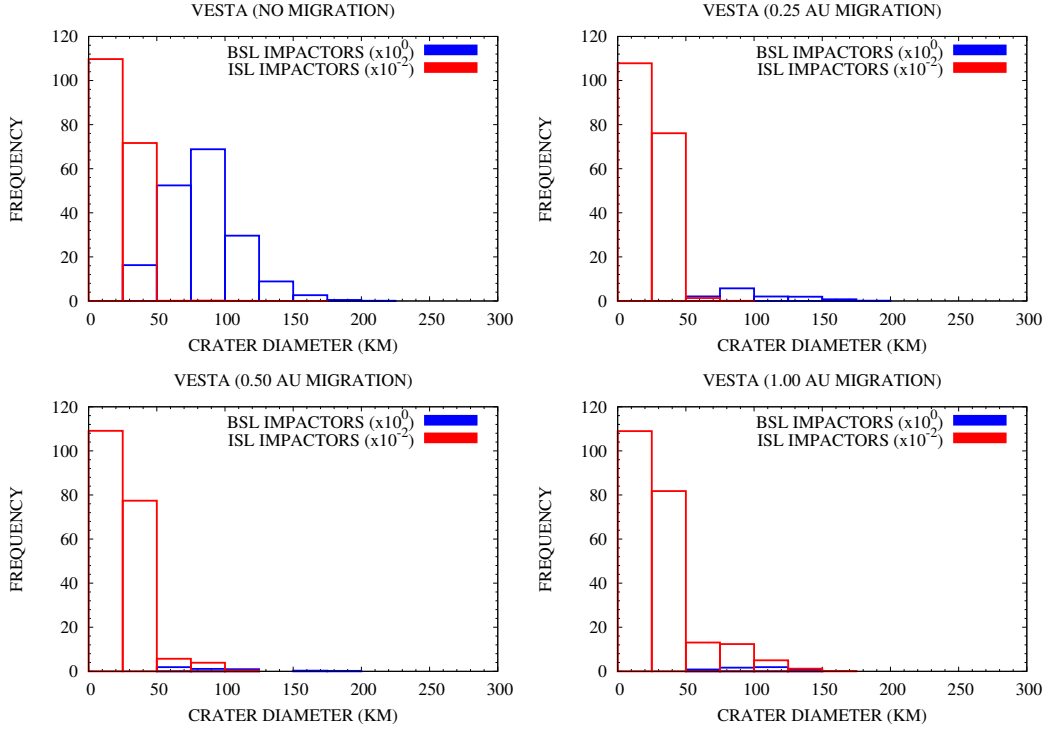


FIGURE 11. Normalised frequency versus crater size histograms of Vesta's impactors: red bars are those related to ISL impactors, blue ones to BSL impactors. The frequency of ISL impactors in all plots has been divided by a factor 100 to enhance the readability of the plots. As can be seen: the high-end tail of the ISL crater size distribution moves towards bigger sizes for increasing values of Jupiter's radial displacement. The high-end tail of the BSL distribution shows a somewhat opposite behaviour and its contribution to the surface cratering is eventually completely masked by the one of the ISL impactors.

asteroids up to sizes of $\approx 100\text{ km}$ (see figs. 11 and 12). BSL-related craters, whose sizes are generally distributed between 50 km and 150 km , are responsible for the high-end tail ($150 - 250\text{ km}$) of the simulated crater distributions (see figs. 11 and 12 taking into account that the ISL-related crater frequencies are divided by 100). More in detail, for both asteroid we observe the following interesting result. In Jupiter's no-migration scenario the high-end tail ($d > 100\text{ km}$) of the crater size distribution is completely due to BSL-related impacts (see figs. 11 and 12, top left panels). For increasing values of the displacement of Jupiter's formation region from its present position, we expect only few BSL-related craters with size greater than 100 km (see

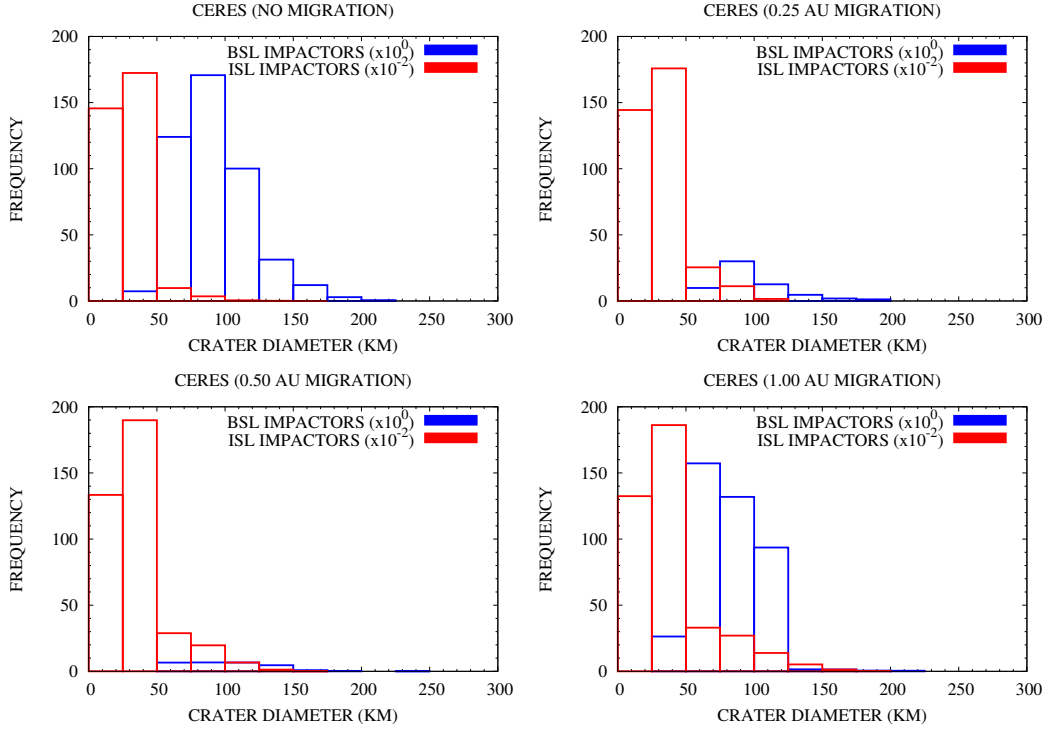


FIGURE 12. Normalised frequency versus crater size histograms of Ceres' impactors: red bars are those related to ISL impactors, blue ones to BSL impactors. The frequency of ISL impactors in all plots has been divided by a factor 100 to enhance the readability of the plots. Similarly to what we observed for Vesta in fig. 11, the high-end tail of the ISL crater size distribution moves towards bigger sizes for increasing values of Jupiter's radial displacement. The contribution of the BSL impactors to the surface cratering is eventually masked by the one of the ISL impactors, with the only exception of stochastic events (see bottom right panel).

figs. 11 12, top right and bottom left panels). At the same time, the high-end tail of the ISL-related crater distribution partially overlaps with the BSL-related crater distribution (ibid). In the 1 AU migration scenario, the high-end tail of the ISL-related crater distribution completely overlap with the BSL-related one, cancelling its contribution in terms of crater frequency (see figs. 11 and 12, bottom right panels). In Ceres' case, we observe that in this migration scenario the contribution of BSL impacts could survive only for crater sizes higher than 200 km (see fig. 12, bottom right panel).

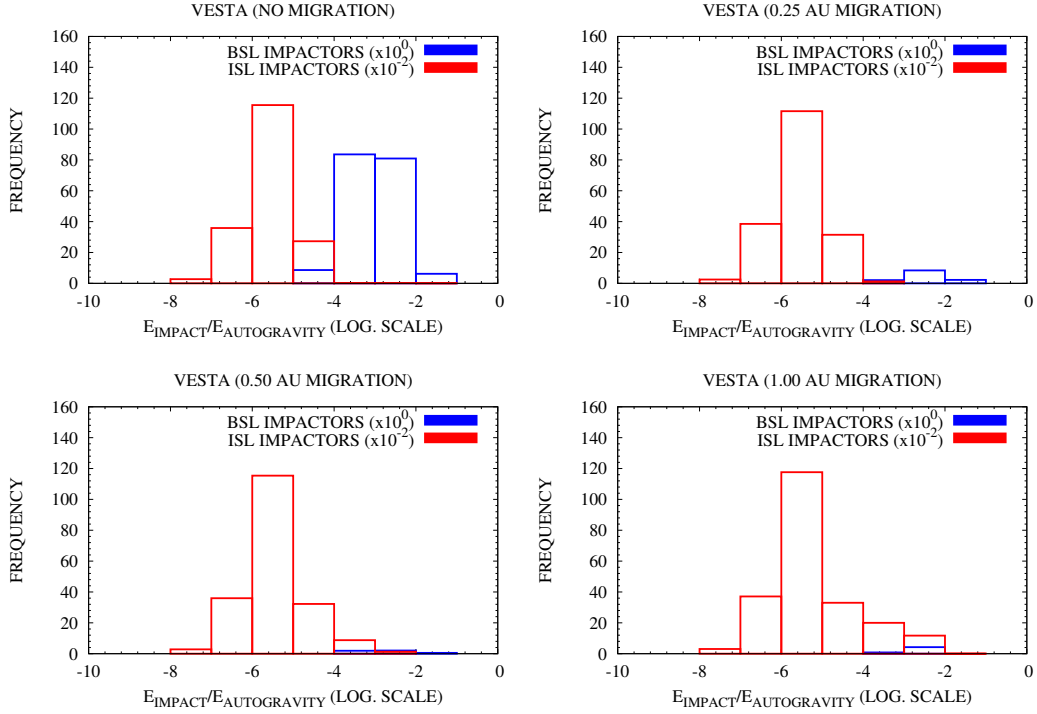


FIGURE 13. Normalised frequency versus impact energy (in units of autogravitation energy) histograms of Vesta’s impactors: red bars are those related to ISL impactors, blue ones to BSL impactors. The frequency of ISL impactors in all plots has been divided by a factor 100 to enhance the readability of the plots. The most energetic impacts (of the order of 10^{-1}) are due to BSL bodies in those scenarios where Jupiter’s radial displacement is limited (no migration or 0.25 AU). ISL impacts in all scenarios and BSL impacts in the 0.5 AU and the 1 AU scenarios are limited to impact energies inferior to 10^{-2} .

3.3.3. *Impact energy.* To evaluate the effects of ISL and BSL impacts on the internal structure of the asteroids, we computed the ratio between the energy delivered by the impacts and the self-gravitation energies of Vesta and Ceres (see figs. 13 and 14). In Vesta’s case the delivered energy spans in the range $10^{-8} - 10^{-1}$ (fig. 13) while in Ceres’ case, due to the greater size of the latter, the range is shifted by an order of magnitude, i.e. between $10^{-9} - 10^{-2}$ (fig. 14). BSL impactors near the frequency peak in their distribution generally deliver 2 – 3 orders of magnitude more energy than ISL impactors at their corresponding peak (see figs. 13 and 14). In analogy to what we observed for the surface cratering, in Jupiter’s no-migration

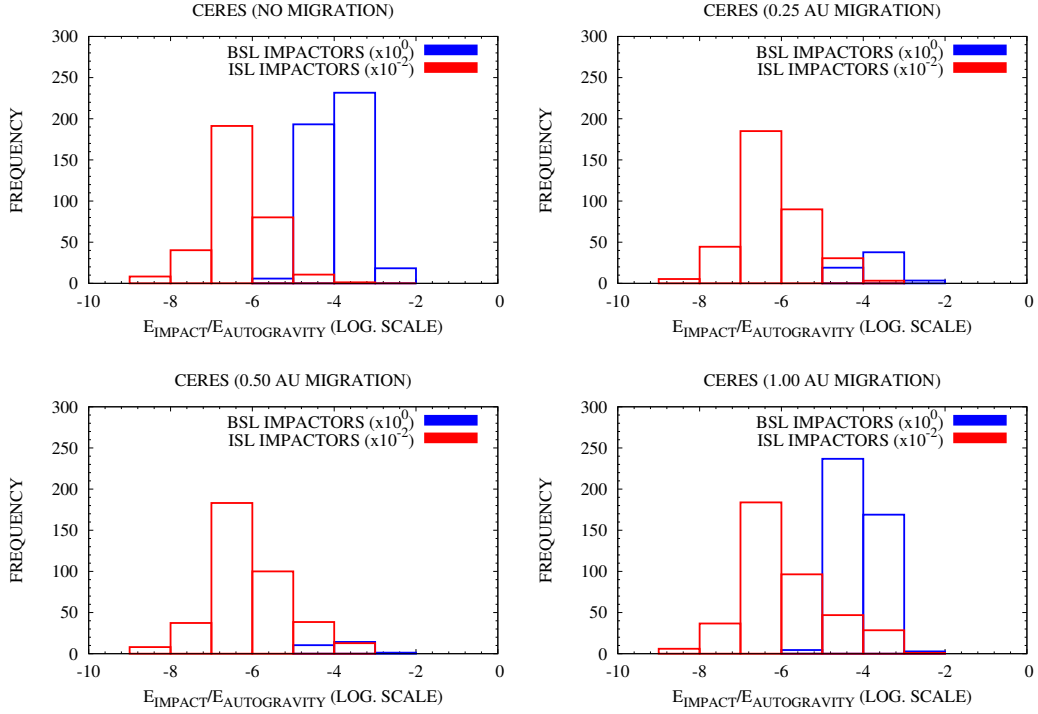


FIGURE 14. Normalised frequency versus impact energy (in units of autogravitation energy) histograms of Ceres' impactors: red bars are those related to ISL impactors, blue ones to BSL impactors. The frequency of ISL impactors in all plots has been divided by a factor 100 to enhance the readability of the plots. Due to the bigger size of Ceres, the impact energies delivered by both ISL and BSL planetesimals in all migration scenarios are of the order of 10^{-2} or inferior.

scenario ISL impacts dominate the low-energy tail of the distribution while BSL impacts are mainly responsible of the high-energy tail (ibid). For increasing values of Jupiter's radial displacement, however, the high-end tail of the ISL distribution shifts toward higher energy values, increasingly overlapping to the BSL distribution (ibid). The contribution of BSL impactors thus become more and more negligible for increasing values of Jupiter's radial displacement and is completely masked by that of ISL impactors in the 1 AU migration scenario (ibid). This effect hold true also in Ceres' case, where the BSL population of impactors is enhanced due to the excitation of a mean motion resonance with Jupiter. From our results it is clearly visible as, due to its smaller size, impacts would deliver on Vesta an higher amount

of energy per units of self-gravitation energy (the high-energy tail being of the order of 10^{-1} , see fig. 13) and are more likely to shatter or significantly fracture the asteroid.

4. DISCUSSION

Our results suggest that the cratering histories of Vesta and Ceres should be strongly correlated to the timescale of Jupiter formation and to its radial displacement. If Vesta or Ceres formed before Jupiter's core reached its critical mass, the expected crater distribution on the surfaces of the two asteroids should show different effects at different times. At the beginning, the crater distribution is dominated by impacts of small rocky bodies that should have lead to an intense and uniform craterisation. These low-velocity impacts could have contributed to the accretion of the asteroids. After Jupiter starts to accrete gas, a second phase of more energetic impacts takes place. Due to their lower number, BSL planetesimals contribute less to the craterisation but, with their higher impact energies, they affect the resurfacing and the thermal histories of the asteroids. A significant fraction of resonant ISL bodies should have impacted the asteroids at supersonic speed, contributing to their excavation and fragmentation. Jupiter's migration should have important effects on this picture, changing the impact speeds and the relative abundances of ISL and BSL populations. The marked dynamical differences between the families of impactors and the strong effect of Jupiter migration should help in interpreting and dating the different features that Dawn will observe on Vesta's and Ceres' surfaces.

REFERENCES

Coradini A., Federico C., Magni G., "Formation of Planetesimals in an evolving Protoplanetary Disk", 1981, *Astronomy and Astrophysics*, 98, 173-185

Magni G., Coradini A., "Formation of Jupiter by nucleated instability", 2004, *Planetary and Space Science*, 52, 343-360

De Pater I., Lissauer J.J., "Planetary Sciences", 2001, Cambridge (UK), Cambridge University Press, ISBN 0521482194

Encrenaz T., "Water in the Solar System", 2008, *Annual Review of Astronomy and Astrophysics*, 46, 5787

Pierazzo E., Melosh H.J., "Understanding Oblique Impacts from Experiments, Observations, and Modeling", 2000, *Annual Review of Earth and Planetary Sciences*, 28, 141-167

INAF - ISTITUTO DI FISICA DELLO SPAZIO INTERPLANETARIO, VIA FOSSO DEL CAVALIERE
100, 00133, ROME

E-mail address: diego.turrini@ifsi-roma.inaf.it

INAF - ISTITUTO DI ASTROFISICA SPAZIALE E FISICA COSMICA, VIA FOSSO DEL CAVALIERE
100, 00133, ROME

E-mail address: gianfranco.magni@iasf-roma.inaf.it

INAF - ISTITUTO DI FISICA DELLO SPAZIO INTERPLANETARIO, VIA FOSSO DEL CAVALIERE
100, 00133, ROME

E-mail address: angioletta.coradini@ifsi-roma.inaf.it